IEEE Photonics Journal
An IEEE Photonics Society Publication

Open Access

Dual-Resonance-Coupling and Sensing Characteristics in an All-Solid Photonic Bandgap Fiber Interferometer Based on LP_{01} Cladding Supermodes

Volume 10, Number 3, June 2018

Wei Huang
Yan-ge Liu
Zhi Wang
Binbin Song
Shengyong Chen

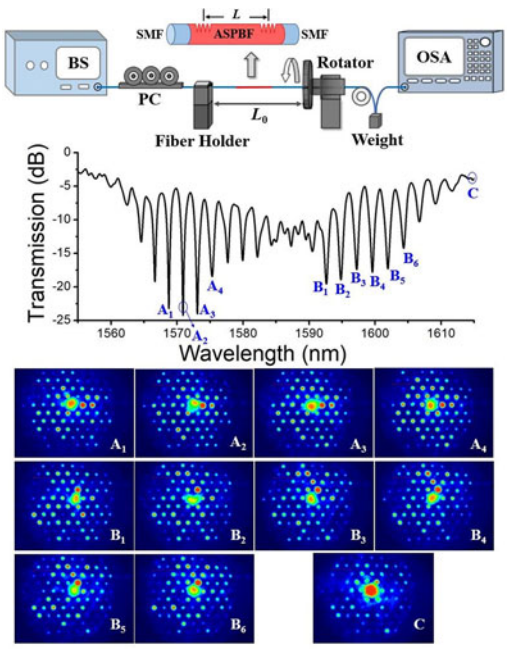

DOI: 10.1109/JPHOT.2018.2846616
1943-0655 © 2018 IEEE

Dual-Resonance-Coupling and Sensing Characteristics in an All-Solid Photonic Bandgap Fiber Interferometer Based on LP_{01} Cladding Supermodes

Wei Huang,[1] **Yan-ge Liu**,[2, 3] **Zhi Wang**,[2, 3] **Binbin Song**,[1] **and Shengyong Chen**[1]

[1]College of Computer Science and Engineering, Tianjin University of Technology, TianJin 300384, China
[2]Key Laboratory of Optical Information Science and Technology, Ministry of Education, Institute of Modern Optics, Nankai University, Tianjin 300071, China
[3]Tianjin Key Laboratory of Optoelectronic Sensor and Sensing Network Technology, Tianjin 300071, China

DOI:10.1109/JPHOT.2018.2846616

Manuscript received April 3, 2018; revised June 5, 2018; accepted June 7, 2018. Date of publication June 12, 2018; date of current version June 18, 2018. This work was supported in part by the National Natural Science Foundation of China under Grants 11704283, U1509207, and 11674177; in part by the Tianjin Natural Science Foundation under Grant 16JCZDJC31000; and in part by the Opening Foundation of Tianjin Key Laboratory of Optoelectronic Sensor and Sensing Network Technology. Corresponding author: Wei Huang (e-mail: emilysnown@163.com).

Abstract: A dual-resonance-coupling phenomenon and the sensing characteristics of an in-fiber modal interferometer based on cascaded long period gratings inscribed in an all-solid photonic bandgap fiber are demonstrated. Theoretical and experimental investigations reveal that the dual-resonance dips result from the coupling between fundamental core mode and two different kinds of LP_{01} cladding supermodes. Due to the deep grooves and asymmetric index distribution along the long period grating caused by side illumination, this dual-resonance interferometer is sensitive to polarization and twist, and the dual-resonance dips according to different LP_{01} cladding supermodes exhibit different responses to twist. Furthermore, the transmission loss and the resonance wavelength of each interference dip show discrimination in sensitivities of temperature and twist, making it a good candidate for multiple physics parameters measurements.

Index Terms: Fiber gratings, micro-optics, sensors.

1. Introduction

Fiber modal interferometric sensors have been extensively investigated in recent years owing to their excellent advantages such as compact structure, flexible and easy to integration, and anti-electromagnetic interference [1]. Various fiber modal interferometric sensors have been proposed by means of long period grating (LPG) pair [2]–[4], fiber taper [5], [6], core-offset fusion splicing or air collapsing technique [7]–[9], and other special fiber structures [10]. To obtain high extinction ratio, the splicing joints of the interferometers constructed by core-offset fusion splicing or air collapsing technique will induce relatively high insertion loss (2–10 dB), and the interferometers composed of tapered fiber also have high insertion loss and the tapered region is relatively fragile. Among them, the LPG pair based fiber interferometric sensors have firm structures, good repeatability, low

insertion loss and easy fabrication. However, the resonance wavelength in LPG-based interferometer is always sensitive to multiple physical parameters, such as temperature, strain, and twist, resulting in cross-sensitivity problem and reduction of measurement accuracy. Therefore, there has always existed the need to develop a new and better approach to discriminate multiple physical parameters simultaneously.

All-solid photonic bandgap fibers (ASPBFs), which confine light in low refractive index solid core by the anti-resonant reflecting optical waveguide (ARROW) effect, have attracted great attention in recent years due to their special and outstanding advantages over conventional fibers [11]–[21]. An ASPBF usually consists of silica background with a periodically arranged high index rods embedded in the low-index background. Different from hollow-core bandgap fibers, the ASPBF can be easily fusion spliced to the conventional fibers without the arc-induced air-hole collapse. What's more, the arrangement of the high-index rods can provide great flexibility to control the light propagating along the fiber, and the cladding Bloch supermodes also exhibit a series of specific optical properties, giving the ASPBF immense potential in high power fiber lasers [12]–[14], nonlinear optics [15], [16] and fiber sensing areas [17]–[21]. More importantly, the special and novel optical properties of Bloch cladding mode in high-index rods provide the potential capability of multi-parameter measurement. Moreover, as a kind of cladding modes, the Bloch supermodes are more sensitive to external conditions. But different from the general fiber sensors which utilize leaky cladding modes as detection modes, the Bloch supermodes bonded in the high refractive index rods are guided modes which have low transmission loss and are more stable and reliable than leaky cladding modes, making it a good candidate for optical fiber sensing measurement.

In this paper, a dual-resonance-coupling phenomenon and the multi-parameter sensing characteristics of an in-fiber modal interferometer based on cascaded long period gratings inscribed in an all-solid photonic bandgap fiber are demonstrated. The cascaded LPGs are inscribed in the same side of the ASPBF simultaneously at the same CO_2-laser pulse condition, so that the parameters of the two LPGs can be as identical as possible. We build a theoretical equivalent model and analyze the dual-intermodal-interference mechanism of the interferometer in detail. With the assistance of LPGs, this dual-resonance interferometer works from the interference between fundamental core mode and two different kinds of LP_{01} cladding supermodes, and the dual-resonance reveals a novel transmission mechanism and optical sensing properties. Due to the deep grooves and asymmetric index distribution along the LPG caused by side illumination, this dual-resonance interferometer is sensitive to polarization and twist, and the interference dips according to different LP_{01} cladding supermodes in the dual-resonance regions exhibit different responses to twist. Furthermore, the transmission loss and the resonance wavelength of each interference dip show discrimination in sensitivities of temperature and twist, making it a good candidate for multiple physics parameters measurements. Moreover, the free spectral range of this interferometer can be controlled simply by adjusting the relative position of the LPGs. This device has many advantages such as firm structure, simplicity, low insertion loss, easy fabrication, compactness, and has potential applications in high temperature conditions [22].

2. Principle and Structure

An all-solid photonic bandgap fiber (ASPBF), produced by Yangtze Optical Fiber and Cable Company Ltd, is employed to fabricate this dual-resonance interferometer. As shown in Fig. 1(a), the ASPBF includes 5 rings of high-index rods encased in index-depressed layers and has very low transmission loss and bending loss. The materials of the high-index rods and the low-index layers are germanium-doped and fluorine-doped silica, respectively. The diameter of this ASPBF is 125 μm, and the average inter-rod spacing is about 9.26 μm. The normalized radii of the high-index rods and the low-index layers around the rods are 0.181Λ and 0.3786Λ, respectively. Their respective average refractive index differences are about 0.028 and -0.008 relative to that of the pure silica background. This PBF can support two kinds of guided modes: the fundamental mode in fiber core and LP_{01} cladding supermodes in the high index rods. Due to the existence of low-index

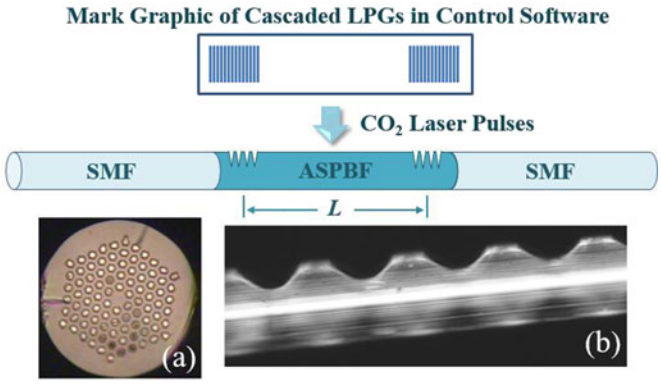

Fig. 1. Schematic diagram of the dual-resonance interferometer fabricated by CO_2-laser side illumination. The two LPGs are inscribed simultaneously at the same side of the ASPBF. (a) The optical microscopic picture of the ASPBF. (b) Microscopic image of the LPG area, and the incident side of the ASPBF is partly ablated while the shadow side is intact.

layers, the LP_{01} supermodes are well confined in high-index rods and are more stable and reliable than common cladding modes.

As shown in Fig. 1, the structure of the proposed dual-resonance interferometer is very simple. Each end of the ASPBF is core-aligned and fusion spliced with two sections of single mode fiber (SMF). Next a pair of cascaded long period gratings are inscribed in the ASPBF to realize the energy exchange between fundamental core mode and different LP_{01} supermodes. L is the distance between the two LPGs. To enhance the extinction ratio of this interferometer, we draw a mark graphic of cascaded LPGs in control software and inscribe the two LPGs in the same side of the ASPBF simultaneously at the same CO_2-laser pulse condition, so that the parameters of the two cascaded LPGs can be as identical as possible. In experiment, the cascaded LPGs are fabricated by use of a focused CO_2-laser beam to notch periodically on one side of the ASPBF. Due to the high-energy laser beam irradiation, the incident side of the ASPBF was deeply grooved while the shadow side is intact, as shown in Fig. 1(b). It's obvious that the LPG region of the ASPBF is non-circular symmetrical.

The resonances between fundamental core mode and LP_{01} supermodes in non-circular symmetrical photonic bandgap fiber are relatively complex. To investigate the mechanisms of the proposed interferometer more systematically, we employed a commercial finite element code (COMSOL) to analyze the optical properties of the coupled modes. As shown in Fig. 2, we calculated the phase-matching conditions and dispersion curves of the fundamental core mode and LP_{01} cladding supermodes of the ASPBF, and the inset pink image in Fig. 2(b) is a typical theoretical equivalent model for the cross-section of the ASPBF after inscribing the cascaded LPGs.

As shown in Fig. 2(a), the bands of LP_{01} cladding supermodes for the equivalent model are bounded by two blue curves, which are the effective refractive indices of the lowest (upper blue curve) and highest order (lower blue curve) of LP_{01} supermodes. Meanwhile, two vector components of LP_{01} core mode are slightly separated due to the asymmetric index distribution along the LPG caused by side illumination. Based on the calculated effective refractive indices of the guided modes and the phase-matching conditions of LPG: $\lambda = \Delta n_{eff} \cdot \Lambda$, the resonance wavelengths between core mode and the group of supermodes can be computed respectively. Here, Δn_{eff} is the effective refractive index difference between the resonance modes, and Λ is the grating period. The red and black lines in Fig. 2 represent the phase-matching curves between the two vector components of LP_{01} core mode and the lowest and highest order of LP_{01} cladding supermodes. If we set the grating period to be 160 μm, the red and black rectangular areas in Fig. 2 represent the resonance regions in wavelengths.

The proposed interferometer works from the interference between the fundamental core mode and LP_{01} cladding supermodes, so the interference spacing of the fringes depends on the

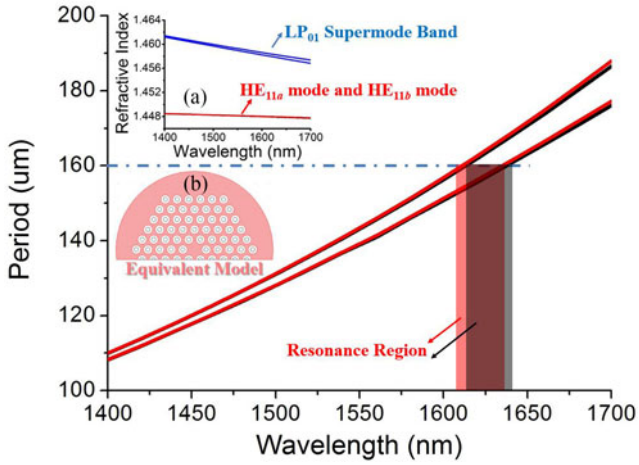

Fig. 2. Phase-matching conditions and dispersion curves of the fundamental core mode and LP_{01} cladding supermodes for equivalent model.

optical path difference (OPD) between the two modes: $OPD = \Delta n_{eff} \times L$. The wavelengths of the interference dips satisfy the phase matching condition:

$$\Delta n_{eff} \times L = \left(m + \frac{1}{2}\right) \times \lambda \tag{1}$$

Where m is an integer. The temperature sensitivity can be calculated from equation (1):

$$S = \frac{d\lambda}{dT} = \lambda \cdot \frac{\Delta n_{eff}}{\Delta n_g} \left(\alpha + \frac{1}{\Delta n_{eff}} \cdot \frac{\partial \Delta n_{eff}}{\partial T}\right) = \lambda \cdot \frac{\Delta n_{eff}}{\Delta n_g} (\alpha + \beta) \tag{2}$$

Where α represents the thermal-expansion coefficient of ASPBF, $\beta = (1/\Delta n_{eff})\partial \Delta n_{eff}/\partial T$ is the effective thermo-optic coefficient, and Δn_g is the group refractive index difference of two modes:

$$\Delta n_g = \Delta n_{eff} - \lambda \cdot \frac{\partial \Delta n_{eff}}{\partial \lambda} \tag{3}$$

In our ASPBF, the thermo-optic coefficients of pure silica, Ge-doped and F-doped silica are $6.9 \times 10^{-6}/^{\circ}C$, $8.6 \times 10^{-6}/^{\circ}C$, and $6.7 \times 10^{-6}/^{\circ}C$, respectively. The thermal-expansion coefficient α is 5.5×10^{-7} for silica [22], which is almost 3 orders smaller than the effective thermo-optic coefficient β (the effective thermo-optic coefficient referring to the fundamental core mode and the highest order of LP_{01} supermode is 1.22×10^{-4} at 1550 nm). So the thermal-expansion coefficient can be neglected and the temperature sensitivity of this interferometer can be predicted. Fig. 3 shows the theoretical temperature sensitivity of this interferometer based on the equivalent model in Fig. 2(b). The black lines in Fig. 3 represent the sensitivities referring to the fundamental even core mode interfered with the lowest (upper black line) and the highest (lower black line) order of LP_{01} supermodes, while the red lines correspond to the fundamental odd mode interfered with the lowest (upper red line) and the highest (lower red line) order of LP_{01} supermodes. Due to the dispersion effect, the temperature sensitivities increase as wavelength increases, and the sensitivities ranges from 68.20 pm/°C to 70.07 pm/°C at 1550 nm for different interfered modes.

As analyzed above, the fundamental core mode can be coupled to different LP_{01} supermodes which meet the phase-matching conditions theoretically. But in experiment, the resonances between core mode and cladding supermodes are more complicated. As shown in Fig. 1(a), the microstructure of the ASPBF is usually imperfect, which will influence the mode distribution located in high-index rods. More importantly, the asymmetric index distribution over the cross section of the LPGs will also have an effect on the properties and electric fields of guided modes, especially the cladding supermodes. According to coupled-mode theory, the resonances between core mode

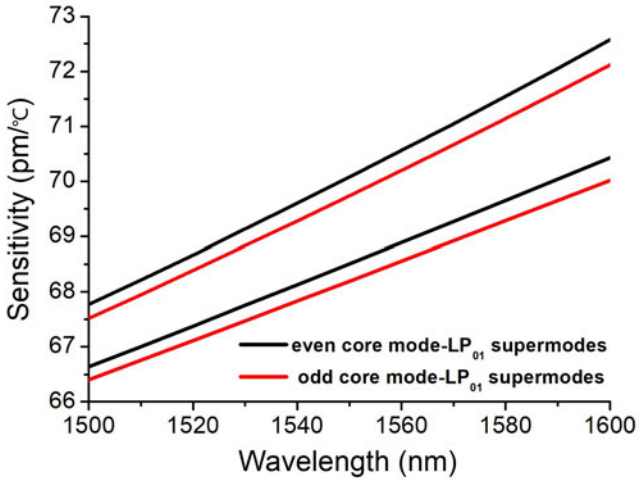

Fig. 3. Calculated temperature sensitivity of the interferometer.

and cladding supermodes will not only depend on the phase-matching conditions we calculated above, but also relate to the overlap integrals of the electric fields between these two modes in the asymmetric ASPBF. Thus, the fundamental core mode can be coupled to only a few supermodes in experiment, and the proposed interferometer is also sensitive to polarization due to the asymmetric structure.

3. Experimental Results

Based on the phase matching conditions, we choose the grating period to be 160 μm and fabricated the proposed interferometer. In experiment, light from a broadband laser source (1460 nm–1620 nm) is launched into SMF and the output transmission spectra is measured by an optical spectrum analyzer (OSA) with the highest resolution of 0.01 nm. A polarizer and a polarization controller are inserted between the broadband source and the interferometer for polarization control. The distance between two LPGs is 40 mm.

As shown in Fig. 4, there are distinct and high contrast interference fringes exist in the spectrum of the proposed interferometer, and the interference fringes range from 1560 nm to 1610 nm. It's obvious that the spectrum exhibits two groups of dips (A and B). The wavelengths of the marked dips are 1568.77 nm (A_1), 1570.92 nm (A_2), 1573.09 nm (A_3), 1575.32 nm (A_4), 1592.64 nm (B_1), 1594.83 (B_2), 1597.23 nm (B_3), 1599.60 nm (B_4), 1601.95 nm (B_5), 1604.34 nm (B_6), respectively. The measured average free spectral ranges (FSR) among dips A_1–A_4 and B_1–B_6 are 2.18 nm and 2.34 nm, respectively. The FSR of these interference fringes also depends on the distance between the two LPGs, so we can control the FSR simply by adjusting the relative position of the LPGs.

To investigate and verify the fiber modes participated in this interference, we employ an infrared charge-coupled device to observe the transmission mode field distribution of the ASPBF after passing through the cascaded LPGs. Fig. 4 shows the near field images of the marked interference dips at different wavelengths. It's evident that the excited cladding modes of the two interfered groups are both LP_{01} cladding supermodes, and the core mode is also confirmed to be fundamental mode. The near field images of the interference dips A_1–A_4 exhibit the same supermode distribution pattern, and the images of dips B_1–B_6 show another kind of supermode distribution pattern. Therefore, a dual-resonance-coupling phenomenon is observed in this interferometer, which comes from the interferences between fundamental core mode and two different kinds of LP_{01} cladding supermodes. We attribute this dual-resonance phenomenon to the deep grooves and asymmetric index distribution along the LPGs. With this special asymmetric structure, the fundamental core mode is easier to be coupled to these two specific types of LP_{01} cladding supermodes. Moreover, this

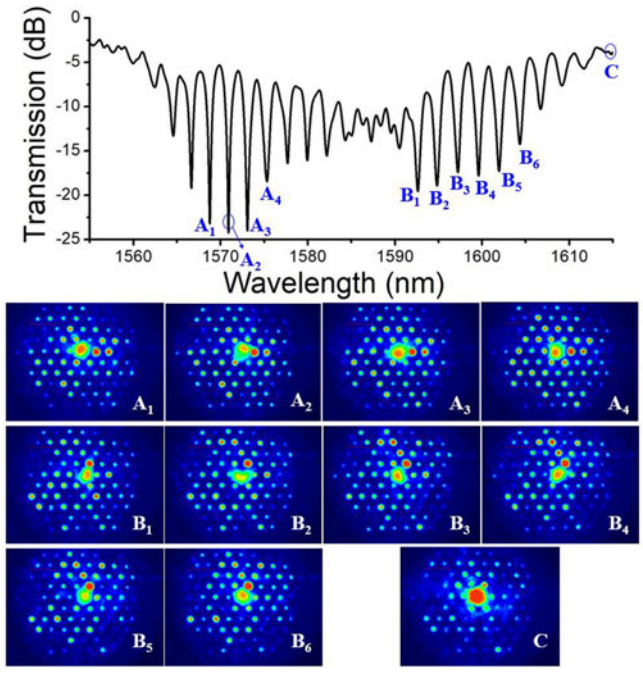

Fig. 4. Measured spectrum of the dual-resonance interferometer and the near field images of each marked dip.

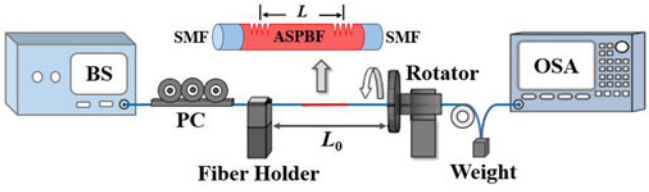

Fig. 5. Schematic experiment setup of the twist sensing system.

dual-resonance interferometer has good repeatability. We repeat this experiment several times and fabricated several interferometers with the same inscription conditions, and the dual-resonance phenomenon can be observed every time.

Owing to the special asymmetric structure, this dual-resonance interferometer is sensitive to polarization and twist. To investigate the sensing properties of this device, we built a twist sensing system, as shown in Fig. 5. This system consists of a broadband source (BS) and an optical spectrum analyzer (OSA), and the polarization controller (PC) is employed to control and maintain the polarization state of incident light. The interferometer fabricated by ASPBF is spliced between two SMFs. One end of the SMF is clamped by a fiber holder, and the other end is mounted at the center of a rotator with an engraved dial embedded to apply twist onto the fiber. The distance L_0 between fiber holder and the rotator is 21 cm.

When the twist is applied to the interferometer, the deep grooves and the asymmetric index distribution along the two LPGs are no longer at the same side of the ASPBF, which will affect the interference strength of each dip. As different LP_{01} supermodes have different mode field distributions, the interference strength responses could be different. The twist effect will also cause refractive index modulation along the fiber axis, but the resonance modes are both guided modes which are well confined in fiber core and the high-index rods respectively. So the twist has less influence on the effective refractive index of the guided modes, and the resonance wavelength shifts can be neglected.

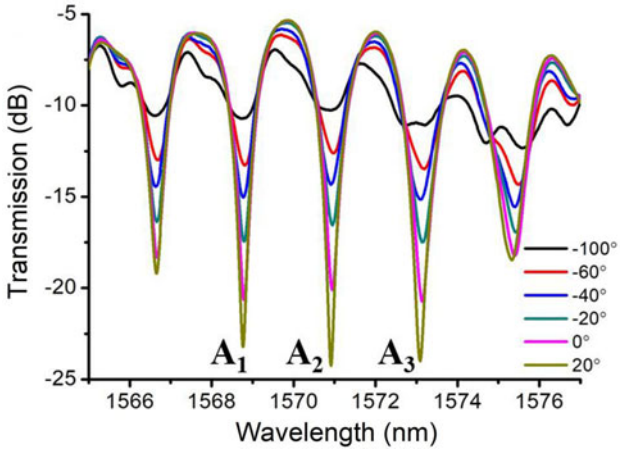

Fig. 6. Transmission spectral characteristics of the left group of dips (A_1–A_3) under different torsion angles.

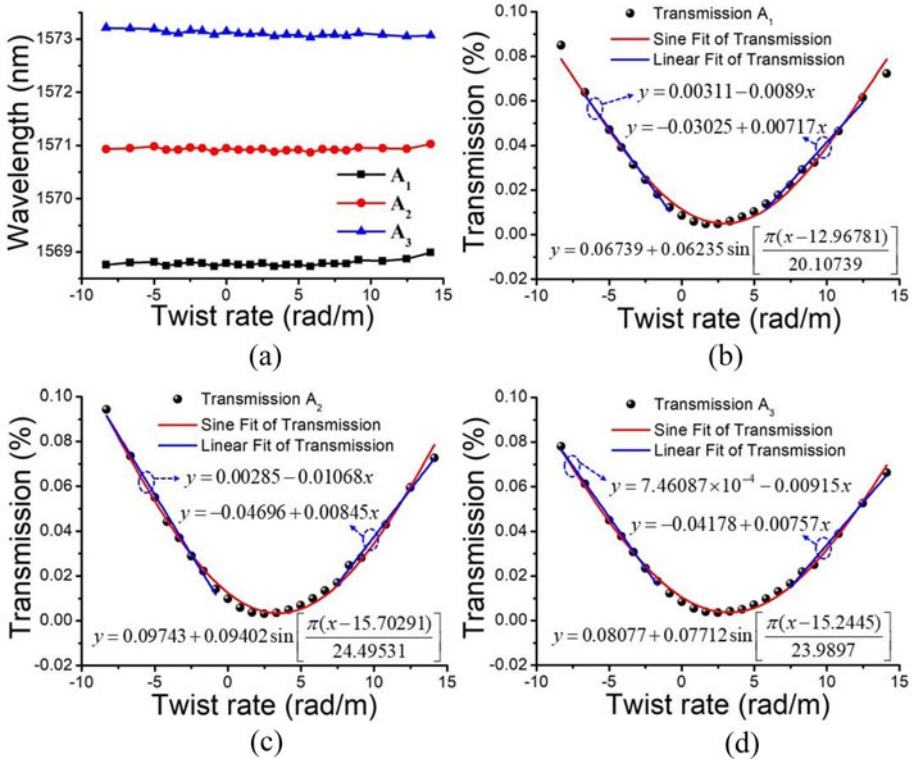

Fig. 7. Torsion responses of the dips (A_1–A_3): (a) wavelength responses; (b)–(d) transmission responses.

In experiment, we investigate the twist responses of the interference dips at different torsion angles. The dual-resonance region of the interferometer shows different spectral responses to the increment of twist. We divide the dual-resonance region into two groups (left group of dips A and right group of dips B) and analyze the sensing properties respectively. Fig. 6 shows the transmission spectral characteristics of the left group of dips (A_1–A_3) under different torsion angles. With the increment of torsion angles, the extinction ratio of each dip in group A varies greatly. Fig. 7 shows

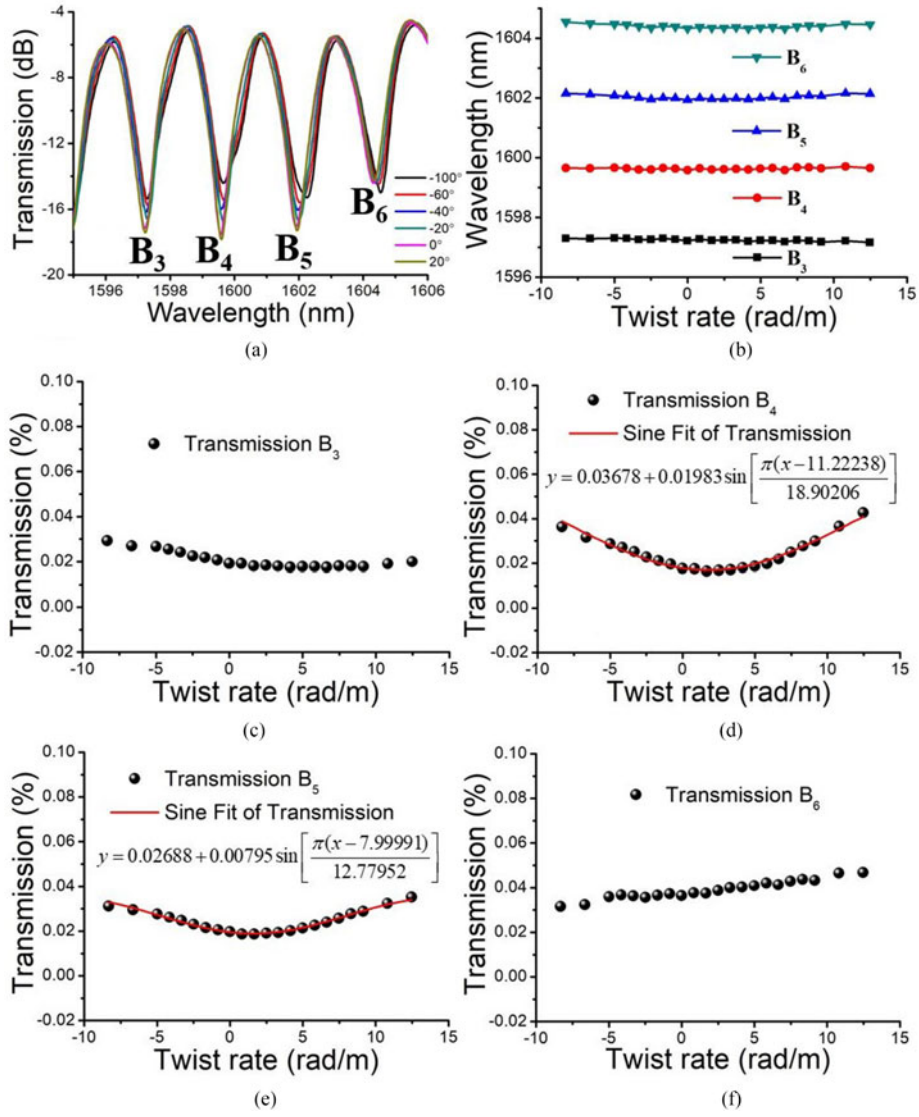

Fig. 8. (a) Transmission spectral characteristics of the right group of dips (B_3–B_6) under different torsion angles. Torsion responses of the dips (B_3–B_6): (b) wavelength responses; (c)–(f) transmission responses.

the wavelength shift and extinction ratio for each dip respectively. As the torsion angle is varied at different points along the fiber axis between the fiber holder and rotator, it's necessary to use $\gamma = \theta/L_0$ to quantify the twist rate. As shown in Fig. 7(b), the red line is the sine fitting with $R^2 = 0.9857$ for the torsion angle ranging from $-100°$ to $170°$ of dip A_1, and the maximum transmission loss variation is 12.54 dB. The blue lines in Fig. 7(b) show the linear fitting of the particular regions, and the transmission loss sensitivities are 0.89%/(rad·m^{-1}) ($R^2 = 0.99473$) and 0.717% /(rad·m^{-1}) ($R^2 = 0.98492$), respectively. The similar responses can be seen in Figs. 7(c) and (d), in which the red lines are also the sine fittings with $R^2 = 0.99159$ (dip A_2) and $R^2 = 0.99461$ (dip A_3), respectively. The maximum transmission loss variation is 14.80 dB for dip A_2 and 13.47 dB for dip A_3 under the torsion angle ranging from $-100°$ to $170°$. Similarly, by linear fitting the particular regions, the blue lines in Fig. 7(c) show that the transmission loss sensitivities are 1.068% /(rad·m^{-1}) ($R^2 = 0.99361$) and 0.845%/(rad·m^{-1}) ($R^2 = 0.99424$) for dips A_2, and Fig. 7(d) shows that the transmission loss sensitivities are 0.915% /(rad·m^{-1}) ($R^2 = 0.99635$) and 0.757% /(rad·m^{-1}) ($R^2 = 0.99199$) for dips

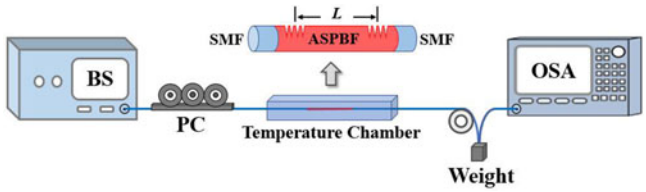

Fig. 9. Schematic experiment setup of the temperature sensing system.

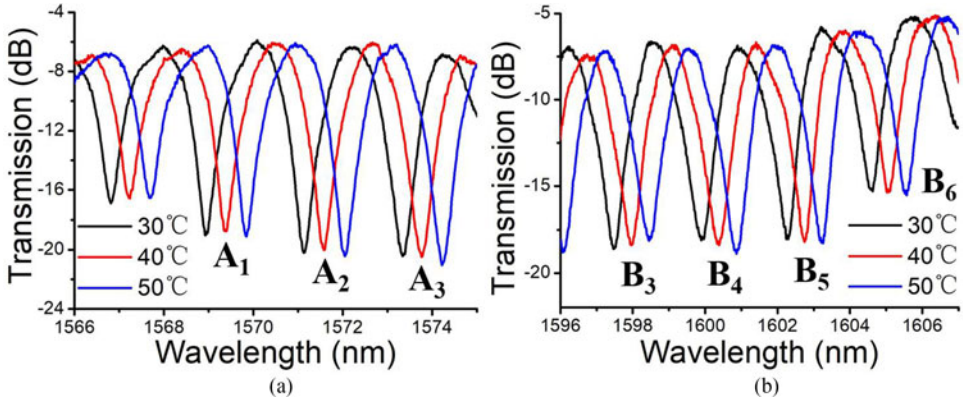

Fig. 10. Transmission spectral characteristics of the two groups of dips under different temperatures.

A_3, respectively. Although the extinction ratio of each dip in group A varies greatly, the resonance wavelengths remains almost unchanged considering the measurement errors in experiment, as shown in Fig. 7(a). The experiment results agree well with our theoretical analysis.

As we demonstrated before, the mode field distribution patterns of the cladding supermodes involved in the dual-resonance region are two different types, so the twist effect has different impact on the two different cladding supermodes. As a result, the transmission loss responses to twist of the two groups of interference dips are also different. Compared with the interference dips of group A, the dips in group B are less sensitive to twist, as shown in Fig. 8. With the torsion angle ranging from $-100°$ to $150°$, the maximum transmission loss variations are 2.22 dB for dip B_3, 4.11 dB for B_4, 2.76 dB for B_5, and 1.67 dB for B_6, respectively. Due to the small changes in transmission loss and the existence of measurement errors, it's hard to fitting the twist sensing data, especially for dip B_3 and dip B_6. The red lines in Figs. 8(d) and (e) are the sine fitting with $R^2 = 0.97223$ (dip B_4) and $R^2 = 0.98112$ (dip B_5) for the torsion angle ranging from $-100°$ to $150°$, respectively. Since the cladding modes involved in the dual-resonance region are both LP_{01} supermodes, the resonance wavelength responses of group A and B are similar. The wavelengths of group B also remain almost unchanged considering the measurement errors in experiment, as shown in Fig. 8(b).

Moreover, the temperature sensitivities of this dual-resonance interferometer are investigated. As shown in Fig. 9, the ASPBF region is placed inside a temperature chamber and the interferometer is heated through atmosphere. The ASPBF is straightened with a constant axial strain provided by a preset load in order to avoid the bending influence. In the heating process, the temperature is increased with a step of 10 °C and stays approximately 15 min in each step for accuracy. The cladding modes involved in the dual-resonance region are both LP_{01} supermodes, so the variation of temperature has similar influence on the interference dips. Fig. 10 shows the transmission spectral characteristics of the two groups of dips under different temperatures. As predicted, the temperature responses for group A and B are similar. The wavelength shifts and transmission losses of the interference dips are both investigated. Different from the twist responses, the interference wavelength of each dip varies greatly with the increment of temperature, while the transmission loss remains almost unchanged.

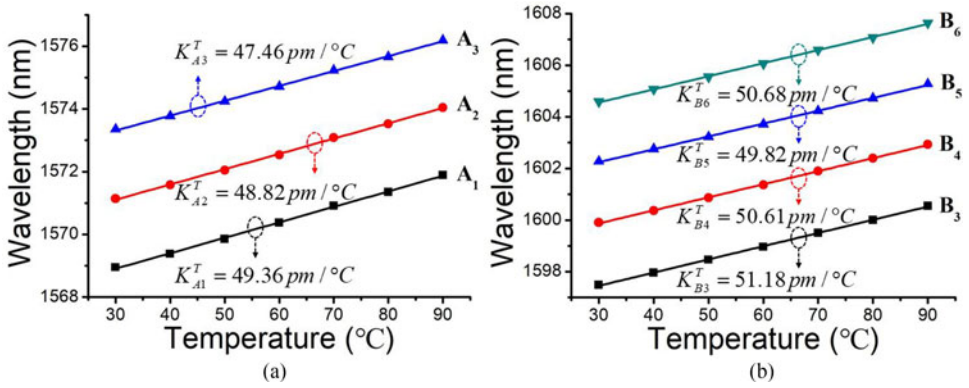

Fig. 11. Wavelength responses of the two groups of dips under different temperatures: (a) A_1–A_3; (b) B_3–B_6.

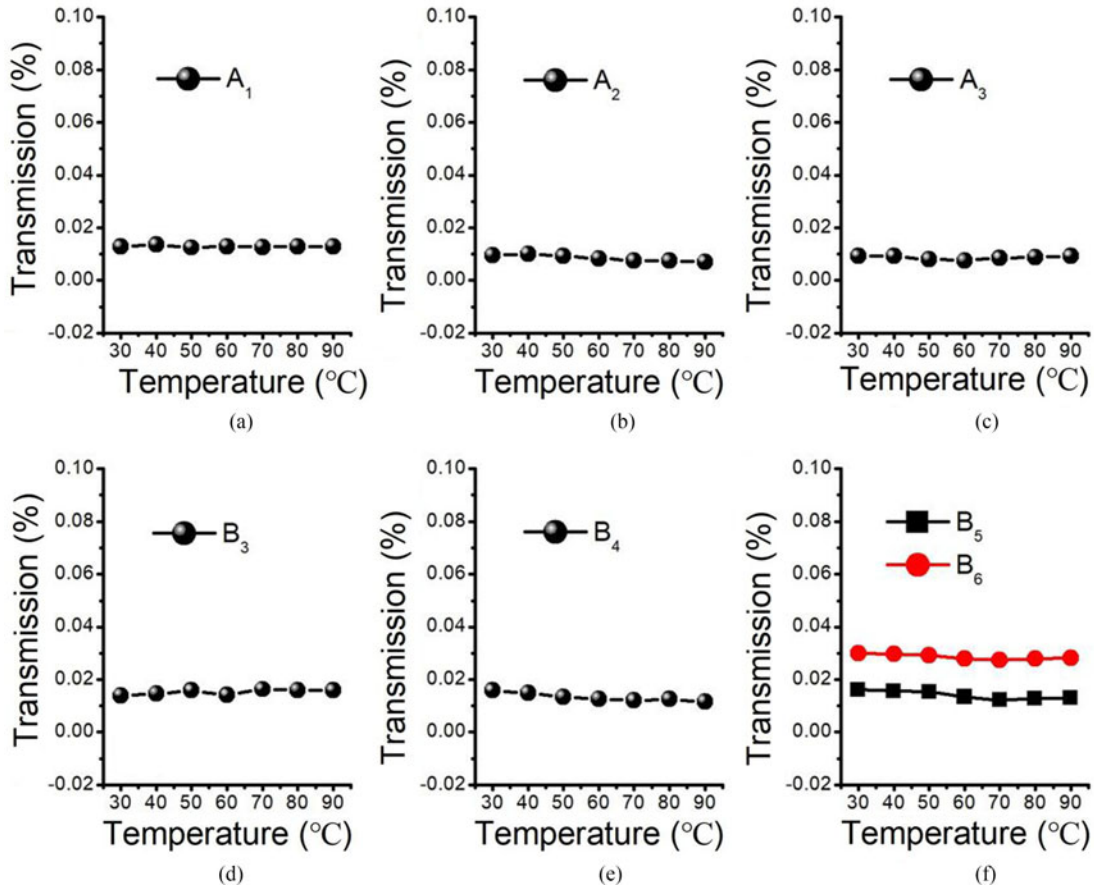

Fig. 12. Transmission responses of the two groups of dips under different temperatures.

Fig. 11 shows the wavelength responses of the two groups of dips under different temperatures. The dips are linearly shifted toward longer wavelengths as temperature increases in the range of 30 °C–90 °C, with slopes of 49.36 pm/°C (A_1), 48.82 pm/°C (A_2), 47.46 pm/°C (A_3), 51.18 pm/°C (B_3), 50.61 pm/°C (B_4), 49.82 pm/°C (B_5), and 50.68 pm/°C (B_6), respectively. The experimental temperature sensitivities are lower than the theoretical sensitivities we calculated above, and we

attribute this to the difference between the equivalent model and the imperfect structure of the ASPBF caused by fabrication. The transmission losses of the marked dips are also monitored as temperature varies, as shown in Fig. 12. With the temperature ranging from 30 °C to 90 °C, the transmission loss variation for each dip remains almost unchanged considering the measurement errors in experiment.

As we demonstrated above, the transmission loss of each interference dip is sensitive to twist while the resonance wavelength keeps almost unchanged as the increment of torsion angles, and the interference dips of group A and B exhibit different responses to twist. Meanwhile, the resonance wavelength of each dip is sensitive to external temperature while the transmission loss keeps almost unchanged. Therefore, this dual-resonance interferometer can deal with the temperature cross-sensitivity problem and has potential applications in multiple physics parameters measurements, especially in simultaneous measurement of twist rate and temperature.

4. Conclusion

In conclusion, we fabricated and demonstrated a dual-resonance interferometer based on cascaded long period gratings inscribed in an all-solid photonic bandgap fiber. This dual-resonance interferometer works from the interference between fundamental core mode and two different kinds of LP_{01} cladding supermodes. We build a theoretical equivalent model and analyze the dual-intermodal-interference mechanism of the interferometer in detail. Due to the deep grooves and asymmetric index distribution along the LPG caused by side illumination, this dual-resonance interferometer is sensitive to polarization and twist, and the interference dips according to different LP_{01} cladding supermodes in the dual-resonance regions exhibit different responses to twist. The transmission loss and the resonance wavelength of each interference dip show discrimination in sensitivities of temperature and twist, making it a good candidate for multiple physics parameters measurements.

References

[1] Z. Liu, H. Tam, L. Htein, M. V. Tse, and C. Lu, "Microstructured optical fiber sensors," *J. Lightw. Technol.*, vol. 35, no. 16, pp. 3425–3439, Aug. 2017.

[2] Y. Li *et al.*, "Bending vector sensor based on a pair of opposite tilted long-period fiber gratings," *IEEE Photon. Technol. Lett.*, vol. 29, no. 2, pp. 224–227, Jan. 2017.

[3] J. Fu *et al.*, "In-fiber M-Z interferometer based on cascaded long period gratings in embedded-core fiber," *IEEE Photon. Technol. Lett.*, vol. 29, no. 21, pp. 1876–1879, Nov. 2017.

[4] T. Hao and K. S. Chiang, "Graphene-based ammonia-gas sensor using in-fiber mach-zehnder interferometer," *IEEE Photon. Technol. Lett.*, vol. 29, no. 23, pp. 2035–2038, Dec. 2017.

[5] B. Sun, F. Fang, Z. Zhang, J. Xu, and L. Zhang, "High-sensitivity and low-temperature magnetic field sensor based on tapered two-mode fiber interference," *Opt. Lett.*, vol. 43, no. 6, pp. 1311–1314, 2018.

[6] J. Li, M. Geng, L. Sun, P. Fan, B. Liu, and B. Guan, "Investigation on single taper-based all-solid photonic bandgap fiber modal interferometers," *Opt. Exp.*, vol. 24, no. 8, pp. 8547–8554, 2016.

[7] M. Bianchetti *et al.*, "Symmetric and asymmetric core-offset mach-zehnder interferometer torsion sensors," *IEEE Photon. Technol. Lett.*, vol. 29, no. 18, pp. 1521–1524, Sep. 2017.

[8] G. Fu, Y. Li, Q. Li, J. Yang, X. Fu, and W. Bi, "Temperature insensitive vector bending sensor based on asymmetrical cascading SMF-PCF-SMF structure," *IEEE Photon. J.*, vol. 9, no. 3, Jun. 2017, Art. no. 7103114.

[9] J. N. Dash, N. Negi, and R. Jha, "Graphene oxide coated PCF interferometer for enhanced strain sensitivity," *J. Lightw. Technol.*, vol. 35, no. 24, pp. 5385–5390, Dec. 2017.

[10] Q. Liu, S. Wang, X. Fu, G. Fu, W. Jin, and W. Bi, "Refractive index insensitive temperature sensor based on waist-enlarged few mode fiber bitapers," *Optoelectron. Lett.*, vol. 13, no. 1, pp. 0025–0028, 2017.

[11] Z. Kakaie, B. H. Shakibaei, Y. M. Sua, D. M. Chow, G. A. Mahdiraji, and F. R. M. Adikan, "Design of single-band bandpass filter using photonic bandgap fiber by suppressing core modes in higher order bandgaps," *IEEE Photon. J.*, vol. 7, no. 3, Jun. 2015, Art. no. 4700214.

[12] S. Li *et al.*, "Cascaded long-period fiber gratings on all-solid photonic bandgap fiber," *Laser Phys.*, vol. 23, no. 6, 2013, Art. no. 065103.

[13] L. Wang, D. He, S. Feng, C. Yu, L. Hu, and D. Chen, "Phosphate ytterbium-doped single-mode all-solid photonic crystal fiber with output power of 13.8W," *Sci. Rep.*, vol. 5, no. 4, 2015, Art. no. 8490.

[14] F. Kong *et al.*, "Polarizing ytterbium-doped all-solid photonic bandgap fiber with $\sim$1150 μm^2 effective mode area," *Opt. Exp.*, vol. 23, no. 4, pp. 1811–1816, 2015.

[15] L. Dong *et al.*, "Large-mode-area all-solid photonic bandgap fibers for the mitigation of optical nonlinearities," *IEEE J. Sel. Topics Quantum Electron.*, vol. 22, no. 2, pp. 316–322, Mar./Apr. 2016.

[16] A. Cavanna *et al.*, "Hybrid photonic-crystal fiber for single-mode phase matched generation of third harmonic and photon triplets," *Optica*, vol. 3, no. 9, pp. 952–955, 2016.
[17] J. Li, M. Geng, L. Sun, P. Fan, B. Liu, and B. Guan, "Investigation on single taper-based all-solid photonic bandgap fiber modal interferometers," *Opt. Exp.*, vol. 24, no. 8, pp. 8547–8554, 2016.
[18] X. Hu *et al.*, "All fiber M-Z interferometer for high temperature sensing based on a hetero-structured cladding solid-core photonic bandgap fiber," *Opt. Exp.*, vol. 24, no. 19, pp. 21693–21699, 2016.
[19] J. Li, P. Fan, L. Sun, C. Wu, and B. Guan, "Few-period helically twisted all-solid photonic bandgap fibers," *Opt. Lett.*, vol. 43, no. 4, pp. 655–658, 2018.
[20] Z. Wu *et al.*, "Supermode bragg grating combined mach-zehnder interferometer for temperature-strain discrimination," *Opt. Exp.*, vol. 23, no. 26, pp. 33001–33007, 2015.
[21] X. Fan, G. Wan, and M. Tong, "Temperature and strain properties of photonic bandgap fiber sensors," in *Proc. IEEE Conf. Progress Electromagn. Res. Symp.*, 2016, pp. 1462–1464.
[22] Y. Geng, X. Li, X. Tan, Y. Deng, and Y. Yu, "Sensitivity-enhanced high-temperature sensing using all-solid photonic bandgap fiber modal interference," *Appl. Opt.*, vol. 50, no. 4, pp. 468–472, 2011.